ICAS-82-6.4.3 EXPERIMENTAL AND THEORETICAL STUDIES OF THREE-DIMENSIONAL TURBULENT BOUNDARY LAYERS ON AN EMPENNAGE OF A TYPICAL TRANSPORT AIRPLANE

H. C. Seetharam, N. J. Pfeiffer,
M. Ohmura and J. D. McLean
Boeing Commercial Airplane Company
Seattle, Washington

Abstract

This paper describes experiments conducted to measure the three-dimensional incompressible turbulent boundary layers on the horizontal and vertical tails of a 1/5 scale model of a transport airplane empennage. The boundary layer measurements were made with a V-shaped anemometer with a high precision traversing mechanism. Variations of angle of attack and Reynolds number were included in the tests. Measurements were also made with small elevator and rudder deflections. The data includes extensive pressure distributions, and detailed analyses of three-dimensional boundary layer data.

Comparison of the experimental data with a three-dimensional boundary layer code taking into account viscous-inviscid interaction is shown. Details of the test theory comparison and the need for a better turbulence model are discussed.

Introduction

Computational fluid mechanics has become an accepted practice in a wide variety of industrial applications. It is extensively used by engineers in various stages of the design process. It has become a basic tool in trade-off studies, parametric evaluation, and incremental effects due to small changes in configurations. It has in part replaced traditional experimental methods such as wind tunnels, which are very expensive and time consuming.

During the last decade, a variety of efficient algorithms were developed to account for viscid and inviscid interactions associated with single and multi-element airfoils, including separation. These techniques are being used as basic tools to analyze and design airfoils specifically tailored to meet desired performance objectives. Extensions of these concepts to analyze three-dimensional problems have been attempted with limited success. Extensive development of panel methods and efficient grid generation techniques have prompted several research workers to develop sophisticated three-dimensional wing boundary layer calculation methods for attached flows and relatively modest loading conditions.

In general, the computational routines for three-dimensional boundary layer computations (Reference 1, for example) are restricted to attached flows. Basically, the methods consist of a potential flow solution coupled with three-dimensional boundary layer equations. Turbulence is simulated by one of the following methods: eddy viscosity, entrainment, one equation and two equation models. Viscous computations are done employing either integral or differential methods and the solution is obtained through an interactive iteration of potential and viscous computations.

As most of the three-dimensional viscous/inviscid routines have emerged from two-dimensional computational technology, there is very limited experimental data available to validate them. Reference 2 provides an excellent overview of the present status of three-dimensional boundary layer computational methods. There are noticable difficiencies in the experimental data; a) uncertainties in the location of transition make it difficult to establish starting conditions for the turbulent boundary layer computations, b) an insufficient number of chordwise and spanwise measurement stations, especially at the trailing edge, to predict the overall three-dimensional characteristics. Since the currently available computational methods cannot handle separated flows, another important consideration is to set up the experimental test conditions for the highest possible lift with attached flow. This results in strong spanwise flows near the trailing edge with incipient separation and is the most demanding test case for the theoretical program. Analysis capability at "off design" conditions is particularly useful in predicting the stability and control characteristics of the airplane.

These requirements were carefully considered in the present tests. Test conditions, model, instrumentation and boundary layer traversing mechanisms were carefully chosen after an extensive development program.

List of Symbols

b = Total Span
c = Local Chord
Cp = Static Pressure Coefficient
Q = Magnitude of Velocity Vector, Local
Q_e = Velocity at the Outer Edge
RN = Reynolds Number
u = Chordwise Velocity Component
u_τ = Friction Velocity
u^+ = Non-dimensional Velocity = u/u_τ
v = Spanwise Velocity Component
x = Chordwise Coordinate
y = Spanwise Coordinate
z = Coordinate Normal to the Local Surface
z^+ = Distance in Wall coordinates = $u_\tau z/\nu$
α = Angle of Attack
β = Crossflow Angle; Positive Outboard
β_e = Crossflow Angle at the Outer Edge
$\Delta\beta$ = $\beta_{surface} - \beta_e$
δ_1^* = Streamwise Displacement Thickness
ν = Kinematic Viscosity
η = Semispan Station = $y/\frac{b}{2}$

Subscripts
B = Body
HT = Horizontal Tail

Test Facility and Experimental Methods

An experimental program was undertaken as a cooperative research effort between the Boeing Company and the Civil Transport Development Corporation of Japan (CTDC). One of the principle attractions was the existance of a relatively large scale empennage model, see Figure 1. The .2 scale model was extensively tested to obtain basic aerodynamic and control surface hinge moment data. Detailed design and model fabrication was undertaken by Mitsubishi Heavy Industries at Nagoya. The model consisted of a horizontal tail with elevators and a vertical tail with full span rudder. The ogival forebody was extended approximately three diameters ahead of the horizontal tail. The aft body was representative of a typical transport airplane including upsweep and side of body flats where the horizontal tail intersects the body.

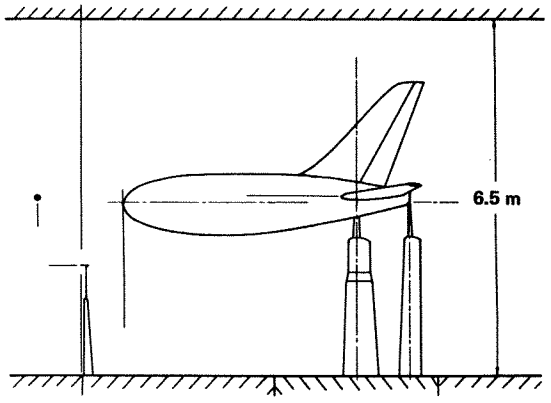

a. SIDE VIEW

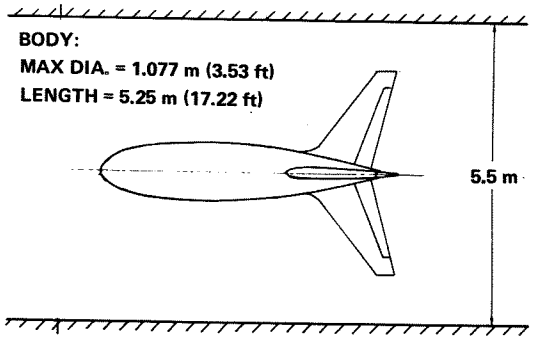

b. PLAN VIEW

	HORIZONTAL TAIL	VERTICAL TAIL
AR	4.5	1.78
SWEEPBACK c/4	32.8°	40°
MAC	.9273 m (3.04 ft)	1.116 m (3.66 ft)
SPAN	3.75 m (12.31 ft)	2.025 m (6.64 ft)
ELEVATOR CHORD	0.3 c	——
RUDDER CHORD	——	0.33c

FIGURE 1 MODEL DETAILS AND INSTALLATION

The model was equipped with 230 surface pressure taps on the horizontal tail and 225 pressure taps on the vertical tail. The pressure taps were equally distributed at five spanwise locations on both horizontal and vertical tails. Additional pressure taps were installed in the trailing edge of horizontal and vertical tails at boundary layer survey stations.

The body was made of fiberglass reinforced plastic formed over a double box steel frame. Horizontal and vertical tails were constructed on a metal skeleton, with the external surfaces made of wood. Details of the model and dimensions are given in Figure 1.

The model was supported by a two strut support system in the 5.5m x 6.5m low speed wind tunnel of the National Aerospace Laboratories of Tokoyo, Japan.

This facility is a single return atmospheric wind tunnel. The tests were carried out with the "semi-closed" configuration, with a small gap between the downstream end of the test section wall and the bell mouth of the first diffuser. The turbulence level was between 0.5 to 0.25 percent in the speed range of the tests.

Experimental Methods

Tests were conducted by using boundary layer trips to ensure transition at 5 percent chord on both suction and pressure sides of the horizontal and vertical tails. Earlier sublimation tests using carborundum grits revealed inconsistent transition patterns. After a series of developmental tests, the following trip configuration was used during the present tests to ensure transition on both sides of horizontal and vertical tails. The trips consisted of 3.3mm (0.13 in) diameter aluminum disks of 0.76mm (0.003 in) thick on the suction side and 0.51mm (0.002 in) thick on the pressure side, spaced two diameters apart. Sublimation tests confirmed the spanwise uniformity of transition.

Boundary layer measurements were made at 5 spanwise stations and 4 chordwise stations on the horizontal tail and 3 chordwise stations and 3 spanwise stations on the vertical tail. All of these measurements were obtained on the suction side only.

The most important part of the test was the proper choice of instrumentation and traversing mechanism. Pressure instrumentation such as a 3 hole yaw probe was not used because of its inadequacy to measure flows with large crossflow angles in a field of relatively high turbulence. Hot wire anemometers are adequate but are affected by contamination in the tunnel such as dust, oil, etc. They are not rugged enough and therefore require extreme care in handling. Hot film anemometers, on the other hand, are rugged and calibrations hold good for a longer period, since the heat transfer properties are less affected by external contamination. The above considerations led to the choice of a V-shaped hot-film probe. The V-probe consisted of two mutually perpendicular sensors arranged in a V-shape. Each sensor's leg was made up of a .001 inch (0.025mm) cylindrical quartz rod with a thin platinum

film deposit. The ends of each rod were attached to gold plated stainless steel support needles. The base of each support needle was anchored into the insulating material at the end of the probe's stainless steel shaft (Figure 2).

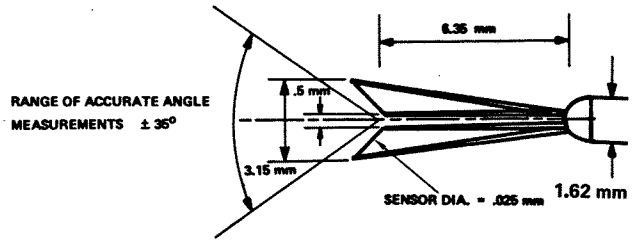

FIGURE 2 V-PROBE HOT FILM SENSOR

Extensive calibration and preliminary testing was done to evaluate the performance limitations of the probes. Calibration was done using a TSI 1125 flow calibrator, modified to allow the probe velocity and angle to be controlled by an HP 3052A system using velocity and angle feedback. Calibration was done at 24 velocities in a range of 5 ft/sec to 400 ft/sec and angle variations of every 2 degrees in the range of ±38°. A fifth order polynomial curve fit was used to compute the velocity magnitude and a third order curve fit was used to compute the flow angle. A standard Lagrangian interpolation scheme was employed to compute velocities and angles from measured anemometer outputs.

Preliminary wind tunnel tests to evaluate the performance of these probes in a realistic test environment revealed that they must be initially aligned accurately with respect to the local slopes--chordwise and spanwise--of the airfoil surface. If the probe is twisted with respect to the local surface, one arm of the probe will be in a different part of the boundary layer than the other arm resulting in erroneous readings. The signals from both arms must be sampled simultaneously since the difference between the two arms is used to measure the flow angle. In a turbulent boundary layer, sequential sampling of the arms was shown to lead to excessive scatter in the flow angle measurements.

Another important phase of the program was a proper choice of traversing mechanism. Main consideration was given to minimum aerodynamic interference of the mechanism and the support system with the airfoil. The most sensitive regions were the measurement stations near the trailing edge. In order to obtain reasonable positioning accuracy, it was necessary to have a rigid support system. This task was achieved by the design and development group of CTDC in consultation with the Boeing Company.

The above considerations led to the choice of a DISA traversing mechanism with a minimum step size of .025mm. For .98c stations, a "spider" type support system (type C) with an appropriate fairing for the traversing mechanism was developed such that the static displacement and amplitude of vibration of the entire system was within .06mm or better as shown in a special wind tunnel test. Simpler, tubular mounts, types A and B, were used at forward stations. The various mounting configurations are shown in Figures 3 and 4.

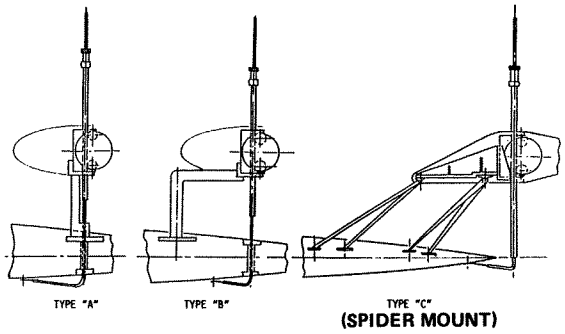

FIGURE 3 TYPES OF TRAVERSE MECHANISM MOUNTS

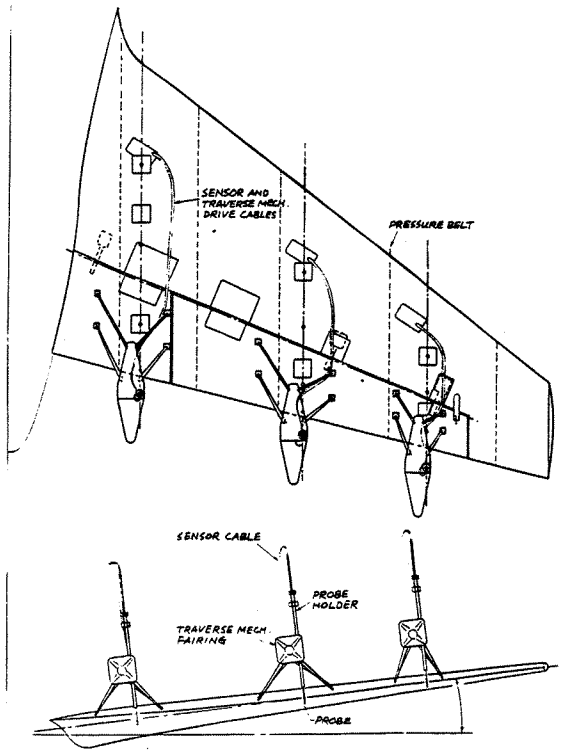

FIGURE 4 TYPE C MOUNTS - INSTALLATION DETAILS

The traverse mechanisms were mounted on the pressure side of the airfoil and the probes were connected to the traverse rod through holes drilled at preselected stations. The probe holding tube was attached to the traverse mechanism while keeping the probe axis parallel to a reference line drawn on the model surface. For .98c stations, the traverse rod was located behind the trailing edge as shown in Figure 3. For high loading conditions, the surface flow angles at .98c stations were expected to exceed the calibration range of the V-probe. Therefore, for these cases, the probe stem was bent by 10°, such that it was aligned inboard 10° with respect to the buttock line. This enhanced the crossflow angle measurement range of -28° to 48°.

The probes were mechanically modified so that the sensing elements were parallel to the local surface. They were then manually positioned so that the sensing elements were .08 to 0.13mm (.003 to .005 in) from the local surfaces depending on the chordwise measurement stations. For horizontal tail tests, five probes were employed at a given chordwise station and positioned at the desired spanwise stations. All probes were traversed simultaneously away from the surface by the same predetermined height increment. The sensor signals were processed and recorded. At each point in the traverse, a rough but quick calculation based on a seven data point sample average was computed for each probe and listed on the printer. This process was repeated up to the last traverse point, which was well above the outer edge of the boundary layer. After the last data point, the probe was returned to the initial position. The probe traversing control was achieved by an HP9825T computer.

Test Conditions

Boundary layer measurements were made at two speeds: 15m/sec and 50m/sec (50ft/sec and 165ft/sec). The two speeds provided a Reynolds number range of 1 to 3 million, based on mean aerodynamic chord. The lower speed case produced a Reynolds number corresponding to low speed developmental tests of typical transport models. Measurements were also obtained with 5 deg. rudder and elevator deflections at a speed of 50m/sec.

Preliminary flow visualization runs were made to select model attitudes in angle of attack and sideslip, such that the surfaces were at maximum loading condition without separation and surface flow angles were within the useful range of the V-probe. The above conditions resulted in sufficiently large crossflow angles, which would provide data for a good test of the capabilities of the three-dimensional boundary layer program.

The sublimation technique with transition disks at 0.05c exhibited a uniform spanwise transition for the critical low lift case ($\alpha_{HT} = -6^{\circ}$). At higher loading case ($\alpha_{HT} = -11.75^{\circ}$), a laminar separation bubble occurred just upstream of the disk location, with reattachment downstream of the disks. The spanwise uniformity of transition was thus ensured for both low and high loading conditions.

In order to provide a good experimental data base for theoretical analysis, most of the test was conducted with a stabilizer incidence relative to the body of -12° instead of a more typical -6°. Higher loading conditions on the horizontal tail were thus achieved with near zero body incidence. This configuration was free from a body vortex interaction with the boundary layer development on the horizontal tail as determined by tests with a simple vortex meter.

The following table gives the details of the test conditions finally selected for the boundary layer tests.

Table 1. Horizontal Tail Test Conditions (Tail Incidence = -12 deg) Zero Sideslip

Vel. m/sec	α_B deg	α_{HT} deg	δ_e deg
15	6	-6	0
15	0.5	-11.5	0
50	6	-6	0
50	-1.5	-13.5	0
50	6	-6	-5
50	1.5	-10.5	-5

Test Procedure

The boundary layer and surface pressure measurements were made with the gaps between tail surfaces and the body sealed, with the exception of tests with deflected elevator and rudder.

Surface pressures were measured for each run by scanivalves employing ±2.5 psid pressure transducers. The pressure data was processed into the pressure coefficient, normalized with respect to tunnel free stream dynamic pressure.

Horizontal tail boundary layer measurements were made simultaneously at five spanwise stations; two measurement stations were positioned on the left hand side of the horizontal tail and three on the right hand side. This was necesary in view of the presence of surface pressure taps on the right side of the horizontal tail. Also, this arrangement worked well since the interference effects between the mounts were minimized. The boundary layer measurements on the vertical tail were made simultaneously at three spanwise locations. For a given condition of tunnel free stream velocity and incidence, there were 20 stations on the suction side of the horizontal tail, and 9 stations on the vertical tail right hand surface.

All probes were initially positioned manually with a feeler guage, and automatically traversed away from the surface by the same height increment.

Details of the traverse control flow chart is shown in Figure 5. Each probe was calibrated briefly using the flow calibrater prior to installation and on removal from the model. This procedure ensured a check on the repeatability of calibration constants and possible drifts due to temperature and contamination.

A maximum number of 28 heights were measured in the boundary layer and 75 data samples were taken at each height. The final velocity and crossflow angles were determined from an average of these 75 data samples. This combination was determined considering the limit of computer capacity and minimum number of samples required to obtain reliable mean values of turbulent boundary layer flow characteristics.

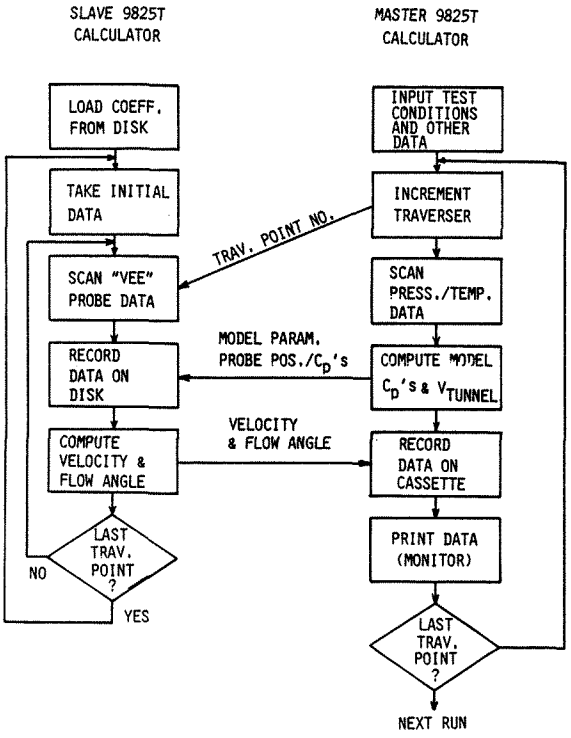

FIGURE 5 TRAVERSE CONTROL FLOW CHART

At the fifth traverse point for each run, data was taken on an analog data tape for dynamic analysis.

During the run, it was felt necesary to take a quick look at the velocity at each traverse point in order to ensure that the last traverse point was well above the outer edge of the boundary layer. This was achieved by an online computation of velocity and angle based on an average of seven data samples and listed on a printer. This process was repeated up to the last traverse point, which was well above the boundary layer outer edge. Typically, each survey took about 40 minutes of tunnel run time. Post test data processing took about 3 to 4 hours. Tabulated listings of the final data based on 75 sample average data of velocity and angle, and plots of velocity and angle profiles were available the same day.

Details of the instrumentation set up for data aquisition and processing is shown in Figure 6.

Comments on Data Accuracy

Positioning

Even though initial positioning was carefully set, some boundary layer profiles exhibited a rather ragged velocity distribution near the surface. In general the probe performance is affected by the local turbulence, proximity to the wall and the mean velocity level. Figure 7 is a typical near wall velocity distribution at .4 and .55 semispan stations, at .2c. The velocity profile at η = .55 shows a familiar distribution, whereas at η = .4 exhibits a

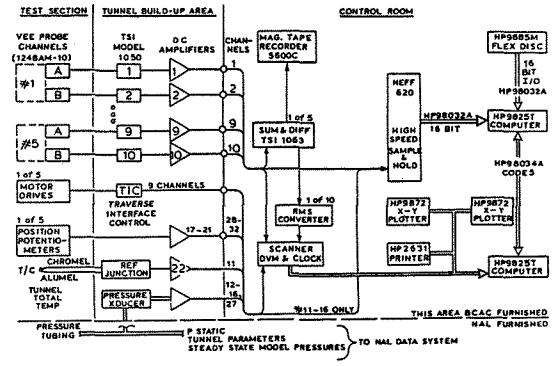

FIGURE 6 INSTRUMENTATION & DATA SYSTEM SET UP

$$V = 15\ M/S, \alpha_B = 6^o, \delta_R = 0^o$$

$$(x/c)_{TRAV.} = 0.20, \eta_{TRAV.} = .40$$

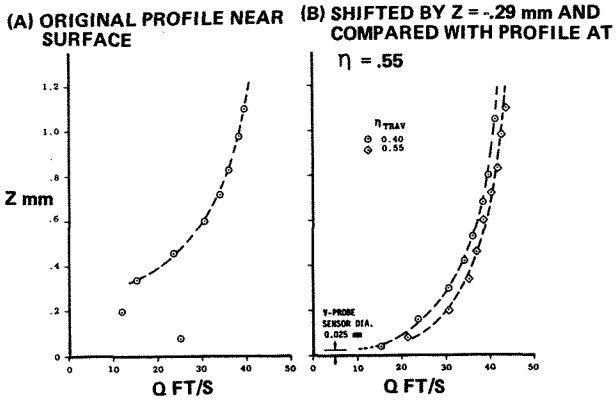

FIGURE 7 PROBE HEIGHT CORRECTION PROCEDURE

rather inconsistant trend near the wall. Eliminating these two points and shifting the height by -0.29mm results in the velocity profile similar to the profile at η = .55.

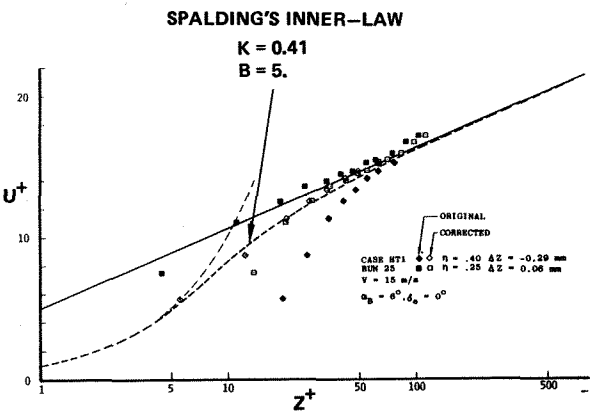

FIGURE 8 LOGARITHMIC REPRESENTATION OF VELOCITY PROFILES

This correction was also substantiated by the logrithmic representation of the measured velocity profiles. Figure 8 shows that the original data collapses on the inner law curve when the probe offset correction is included. This procedure was carried out for each profile and corrections were applied whenever necessary. It should be noted that the velocity and angle profiles shown in the later section do not include the height correction but this correction was accounted for in the evaluation of integral properties.

Surface Pressure Measurements

Independent measurements with pressure transducers of different sensitivity (2.5 psid, and .25 psid range) indicated excellent repeatability of surface pressures. Overall accuracy was in the range of ±.05 to .02 percent.

Comparisons of the velocities derived from the surface pressures with the outer edge velocities measured from the V-probe indicated slight discrepancies. Calibration coefficients obtained between pre and post test exhibited some differences. Calculation of velocities using the two sets of coefficients resulted in values within 5 percent. This was attributed mainly to oil contamination of the probe during the tunnel run. Maximum velocity measurement uncertainty was about ± 5 percent. Some repeat runs were made to complete the data set. The velocities were repeatable within ±1 percent.

The crossflow angle measurement results indicated a rather large scatter near the surface. This is because the flow angle is computed from the difference between the two sensor signals. Another factor contributing to the scatter is the limitation on the total number of samples employed for average computation. In spite of this, the angle measurements were repeatable with ± 1°.

Table 2 shows the overall accuracy estimates.

Table 2. Accuracy Estimates

Angle of attack and sideslip	±0.05°
Dynamic pressure	±0.6 percent
Pressure coefficient	±0.03 percent
Probe positioning initial	-0.3 (mm max)
Probe orientation - initial	±1°
Probe velocity	±5 percent (max)
Crossflow angle, repeatability	±1°

Correction to angle of attack = -.3 to -.85 deg. (Blockage and streamline curvature)

Results and Discussion

The results are presented for the case of horizontal tail incidence of -13.5 deg and at Reynolds number of 3 million. For this case, theoretical results are included. Typical spanwise boundary layer development at selected chordwise stations are also shown at the tail incidence of -6 deg and at Reynolds numbers of 1 and 3 million.

Pressure Distributions

Model surface pressure distributions were recorded during each survey. While the model geometry was essentially the same, the difference was due to the chordwise location of the traverse mechanisms and mounts. Pressure distributions are practically undisturbed by the traverse mechanism and mounts (Figure 9).

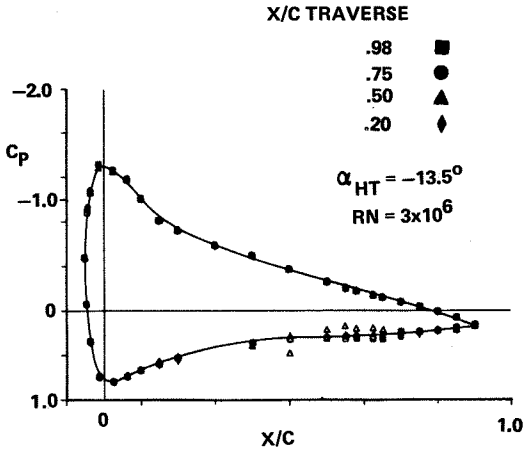

a. η = .22

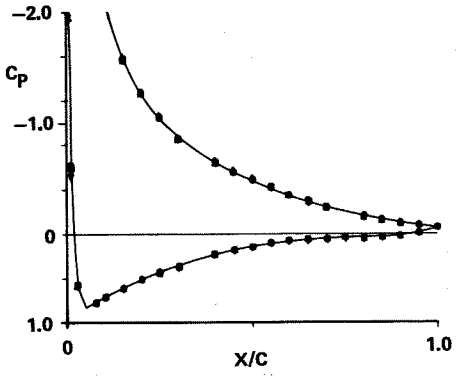

b. η = .90

FIGURE 9 EFFECTS OF TRAVERSE MECHANISM ON PRESSURE DISTRIBUTIONS

Slight scatter was observed on the pressure side, near 0.05c (the trip location) and near the hinge line at 0.7c. Figure 10 shows the suction side pressure distributions at various

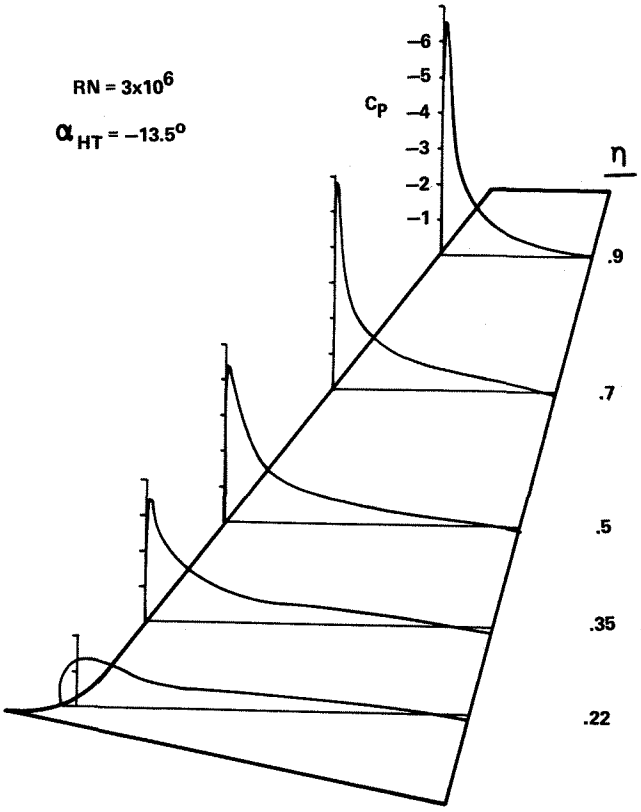

FIGURE 10 EXPERIMENTAL PRESSURE DISTRIBUTIONS

spanwise stations. The pressure distribution at η = .22 does not have a strong suction peak due to the presence of the body. The outboard stations experience considerable acceleration near the leading edge. The trailing edge pressure at η = .9 has a very slight negative pressure coefficient, which is indicative of trailing edge separation onset. Pressure distributions at constant longitudinal stations along lines perpendicular to the plane of symmetry are shown in Figure 11. The leading edge suction causes a negative pressure gradient in the spanwise direction. The adverse chordwise gradient decelerates the fluid in the boundary layer and the negative spanwise pressure gradient bends the direcion of the surface flow more and more towards the tip as the fluid approaches the trailing edge. This is illustrated in the plot of spanwise crossflow variation in Figure 13. A striking aspect of the velocity vectors in the boundary layer is their skewing as the height varies from the surface to the edge of the boundary layer. This twisting is illustrated in the plan view polar velocity vector plots shown in Figure 14. The vorticity associated with this skewing is perpendicular to the surface and

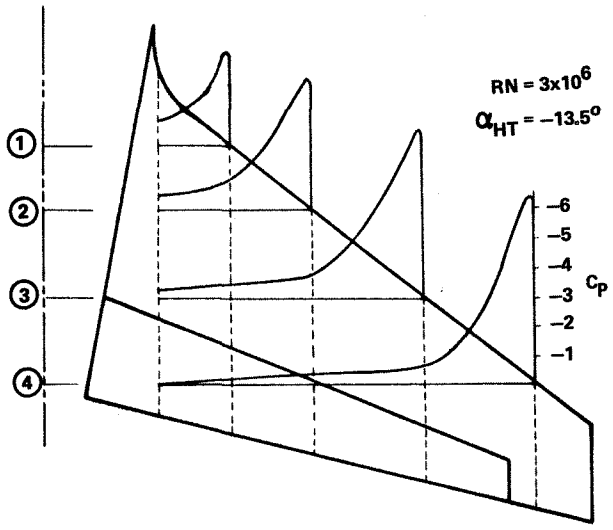

FIGURE 11 SPANWISE PRESSURE DISTRIBUTIONS

combines with the vorticity induced by the shearing action of the boundary layer. At some higher angle of attack than measured during the present test the flow separates. Other experiments for this and similar planforms have shown that maximum lift is associated with the formation of vortical flows. At this time we do not understand how these flows come about and how separation on the aft part of the airfoil interacts with these flows.

Boundary Layer and Crossflow Angle Profiles

At upstream survey stations (as far aft as .5c), experimental velocity vector profiles (Figure 12) exhibit similarity with two-dimensional turbulent boundary layer profiles, with very little departure from the 1/7 power law. This is to be expected, since the net crossflow angles are less than about 15 deg. The boundary layer grows towards the trailing edge due to the strong influence of the adverse pressure gradient. The boundary layer thickness across the span is practically constant, whereas crossflow angles increase considerably. Near the surface, the crossflow angle data exhibits considerable scatter, but the profiles themselves show a systematic variation. The crossflow angles at the outer edge of the boundary layer differ considerably, especially in the inboard regions (up to about η = .4). Also, upstream stations (.2c) have the largest crossflow outer edge angle. Proximity to the body is probably the cause of this feature. Some additional insight into the spanwise trend was obtained by plotting the net crossflow angles ($\Delta\beta = \beta_{surface} - \beta_{edge}$) as shown in Figure 13. This figure shows a systematic and near linear variation of flow angles with span. Again .98c stations depart significantly from the linear variation.

Polar representation due to Johnston (Ref. 3) is often used to obtain a useful picture of the crossflow field. In this case, local velocity

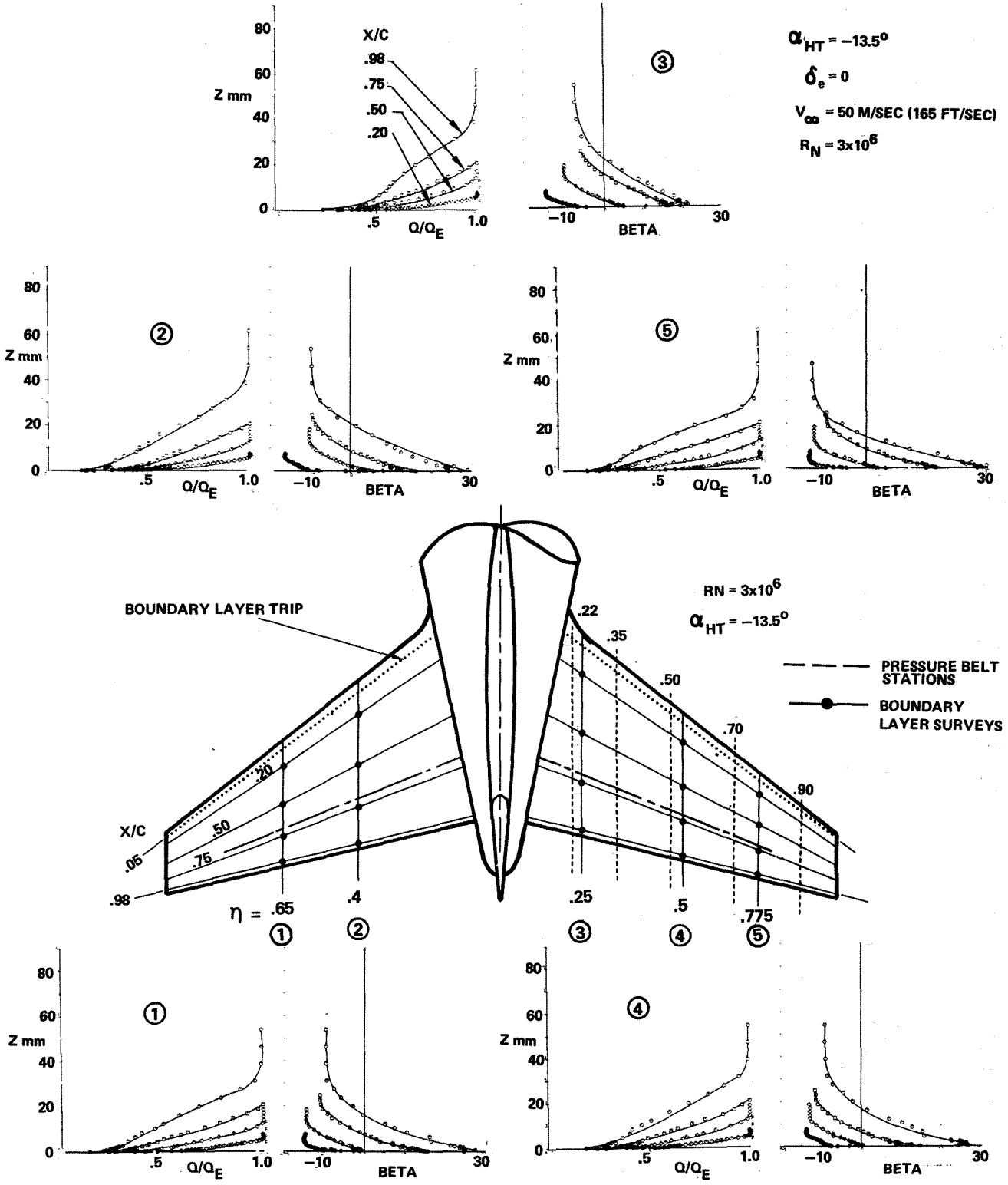

FIGURE 12 EXPERIMENTAL VELOCITY AND CROSSFLOW ANGLE PROFILES

vectors are projected onto the plane tangential to the measurement surface producing a plot of v against u. This "triangular" model is also used by the theoretical researchers with some modification (for example, Ref. 3). A typical example of this type of representation is shown in Figure 14 from the data obtained at five spanwise stations and at .98c. All profiles except η = .4 have a well formed apex (indicating a maximum crossflow angle). The data at η = .4 has a very flat "apex" indicating a substantial departure from the two straight lines. The reasons for the appearance of a sharp apex in some cases and not in others are not clear. Some authors relate the appearance of the peak to the rapid rates of skewing

within the boundary layer.

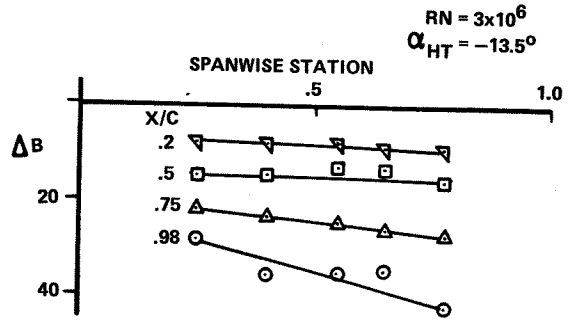

FIGURE 13 SPANWISE VARIATION OF CROSSFLOW ANGLES

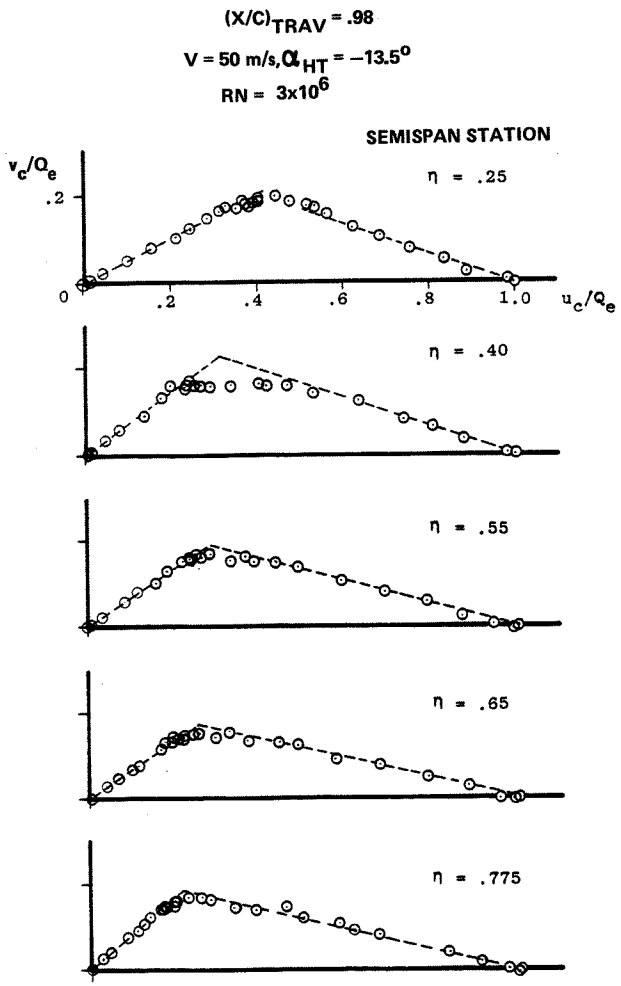

FIGURE 14 POLAR REPRESENTATION OF VELOCITY PROFILES

In view of relatively sparse data, it is rather difficult to develop stream line patterns of surface and outer edge flow. However, the overall picture of local surface and outer edge directions are shown in Figure 15.

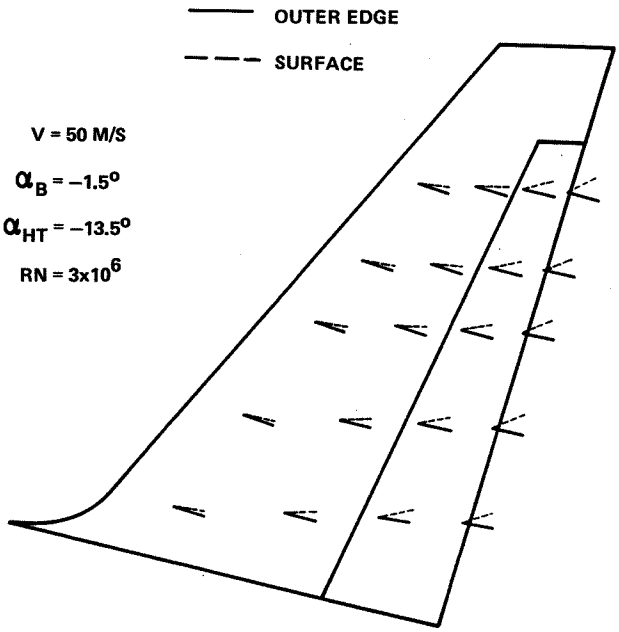

FIGURE 15 LOCAL FLOW DIRECTIONS

Displacement Thickness

It is generally not easy to assign well defined physical meanings to various definite integrals relative to displacement and momentum defects in three-dimensional boundary layer flows. The concept of dislacement thickness and its physical interpretation is given in Lighthill's paper (Ref. 4). In this paper only the familiar two-dimensional equivalent, streamwise displacement thickness δ_1^* is presented (Figure 16). This provides a graphic picture of streamwise development of boundary layer thickness. Note that vertical heights are shown in actual millimeters computed from the streamwise velocity profiles. The spanwise variation of the integral thickness is practically negligible, whereas the streamwise thickness grows rapidly as it approaches the trailing edge. Notice again a slightly thicker streamwise displacement thickness at η = .40 trailing edge, as indicated by the velocity profiles.

Reynolds Number Effects

One of the goals of this research was to obtain the boundary layer characteristics at two Reynolds numbers (1 million and 3 million and at the same incidence of body and horizontal tail (α_B = 6° and α_{HT} = -6°). For comparison, two chordwise stations (.2 and .98) at two span stations of η = .25 and .775 have been shown in Figure 17. The boundary layer profiles indicate substantial velocity defect at low Reynolds number and are slightly thicker. The table below shows the comparison of the streamwise displacement thicknesses computed from the velocity profiles.

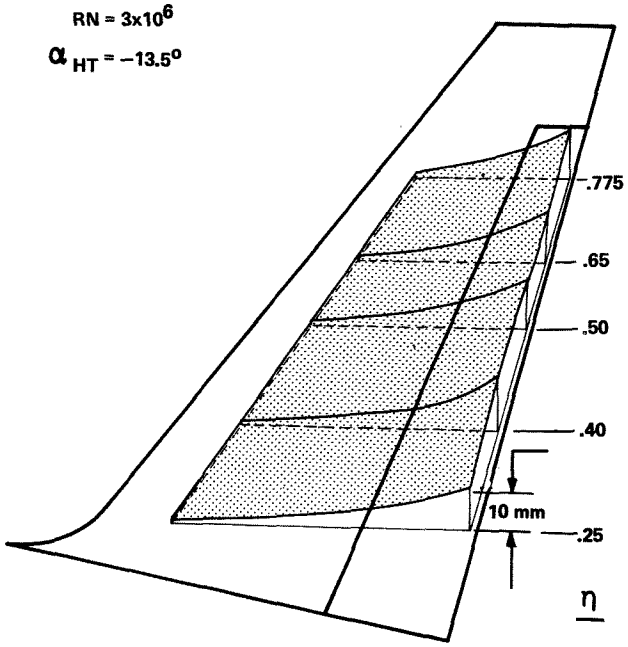

FIGURE 16 STREAMWISE DISPLACEMENT THICKNESS DISTRIBUTION

Table 3. Displacement Thickness Distribution

	δ_1*mm at RN=1x10^6		δ_1*mm at RN=3x10^6	
η/x	.2c	.98c	.2c	.98c
.25	1.14	6.98	.775	5.45
.775	.846	5.22	.568	3.99

The angle profiles do not indicate any systematic Reynolds number variation, except that the surface flow angles at low Reynolds number have slightly higher outboard crossflow.

Computational Results

Detailed boundary layer profiles were calculated for the horizontal tail at a Reynolds number of 3x10^6. The basic computational grid was set up with horizontal tail incience set at -12° with respect to body. The body incidence was selected to match the experimental lift obtained at α_B = -1.5° and α_{HT} = -13.5° (corrected α_B = -2.35° and α_{HT} = -14.35°, see Table 2). The computational body incidence required to match the experimental lift was α_B = -2.7° and α_{HT} = -14.7°. This was the largest negative angle at which all of the experimental stations indicated attached flow.

Computations were made using a system of routines which interfaces a three-dimensional finite difference boundary layer program [1] with a three-dimensional flow code [5]. A brief description and some results of an early

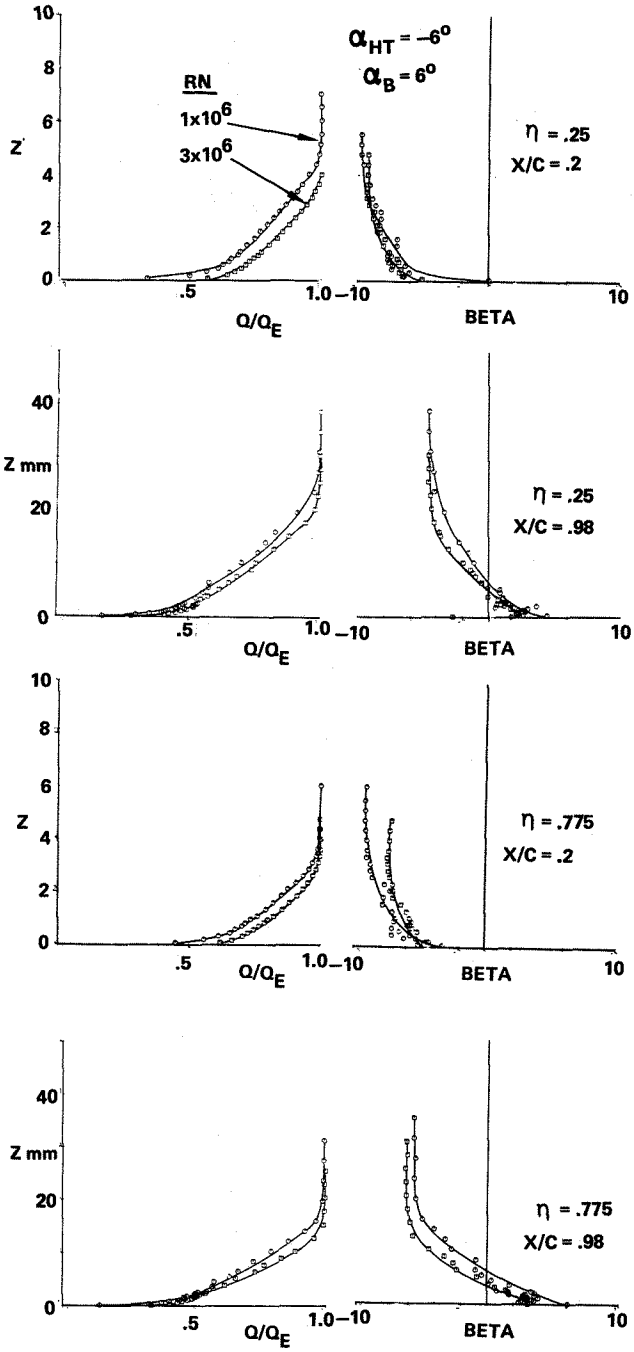

FIGURE 17 REYNOLDS NUMBER EFFECTS ON BOUNDARY LAYER & CROSSFLOW PROFILES

version of this system were presented in Reference 6. This system was chosen for the analysis because of its automatic interfacing which made running the problem less complex.

The potential flow computation grid for the problem is shown in Figure 18. Calculated pressure distributions obtained after three iterations between the potential and boundary layer routines are compared with experimental values in Figure 19. This comparison shows excellent agreement except at the most inboard station where viscous effects due to the body reduce the experimental suction peak.

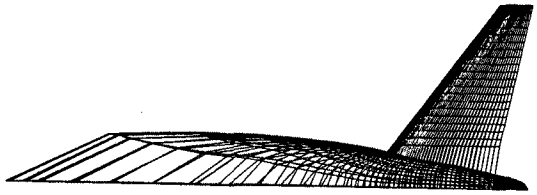

FIGURE 18 POTENTIAL FLOW COMPUTATIONAL GRID

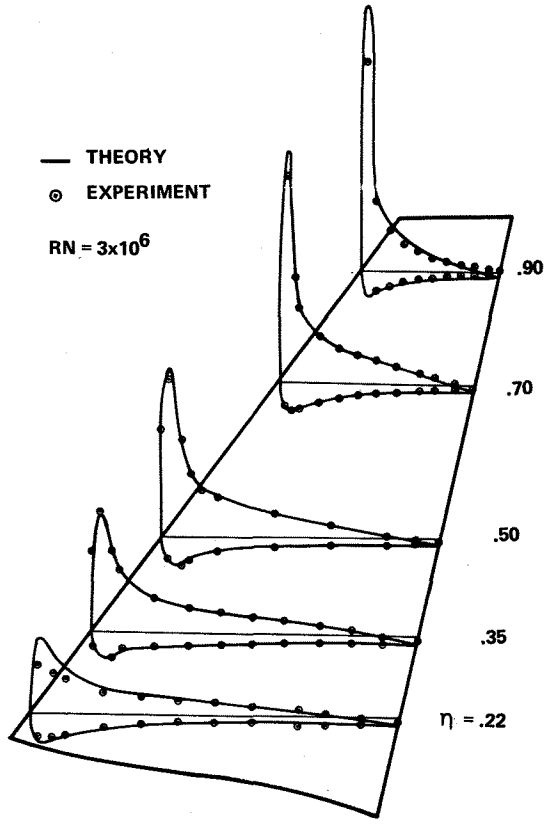

FIGURE 19 PRESSURE DISTRIBUTION: EXPERIMENT & THEORY

The boundary layer calculations use a completely different grid (Figure 20) which is far more dense than that used in the potential flow calculations. The interface routines interpolate values from one grid to the other. The actual boundary layer routines include calculation of an attachment line, determination of wing root initial conditions, laminar boundary layer calculation, transition prediction, and turbulent boundary layer calculation.

Calculated values of flow velocity and angle are compared with experimental results for various spanwise and chordwise positions on the tail in Figure 21. At the forward chordwise

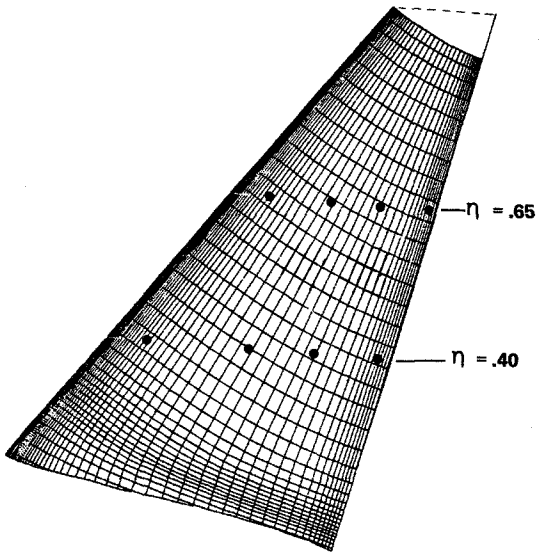

FIGURE 20 GRID FOR BOUNDARY LAYER COMPUTATIONS

positions, the experimental and calculated values match well. Midway aft on the tail, the calculated velocity profiles tend to be slightly fuller than the experimental ones. There is also more deviation in flow angle than at the forward stations. Near the trailing edge, the calculated velocity profiles are definitely fuller than the experimental values. The calculated flow angles deviate appreciably as well. It should be noted that at all locations the boundary layer thickness is well predicted.

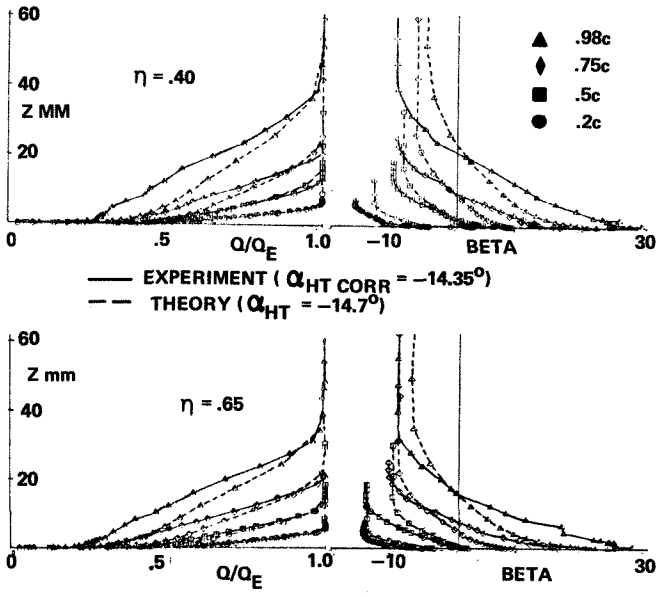

FIGURE 21 COMPARISON OF BOUNDARY LAYER AND ANGLE PROFILES WITH THEORY

The deviation of the calculated values from the experimental results may be due to a combination of errors in both the boundary layer routines and the potential flow calculations. The calculation of flow angle through the boundary layer is clouded due to differences in the computed and experimental flow angles at the edge of the boundary layer. The potential flow routine calculates the flow direction at the outside of the viscous region. Since this direction deviates from the experiment, the boundary layer flow angles are probably affected by the potential flow program itself and indirectly by calculating the potential flow with slightly erroneous boundary layer thickening.

The calculation of boundary layer profiles in the presence of a moderate adverse pressure gradient, tends to yield fuller profiles than are experimentally observed. This effect is accentuated as the flow moves aft toward the trailing edge. It is felt that this fullness is due to the limitations of the current algebraic turbulence model. Further work has been scheduled to examine the effect of turbulence model modifications on the results.

Overall, the boundary layer effect on the outer potential flow has been well modeled for this rather severe angle of attack. This was shown by Figure 19 mentioned earlier. In addition, the calculated thickness of the boundary layer compares favorably with experimental results. It is only when the detailed velocity profiles within the boundary layer are examined that any sizable differences are noted. These differences are most pronounced near the trailing edge, but even then they are not grossly in error. However, these discrepancies throw doubt on the capability of the program to predict separation.

The current boundary layer technique provides good results which allow the calculation of accurate wing pressure distributions for attached flows. The detailed velocity profile information that is calculated by the program is at worst a qualitative match for the case tested with significant adverse pressure gradient. Changes in the viscosity model are planned, however, which should create a better match.

Conclusions

- Detailed pressure distribution and three-dimensional boundary layer data have been obtained on a moderately swept horizontal tail.
- Experimental data shows very little spanwise growth of boundary layer thickness, with substantial chordwise growth.
- Crossflow angles increase considerably towards the trailing edge.
- The theoretical program does an excellent job in predicting the pressure distribution.
- The boundary layer velocity profile is well predicted for upstream stations, but agreement is not good for downstream stations. The theory predicts fuller velocity profiles compared to the experimental data. However, the overall boundary layer thickness is well predicted. Similar trends are exhibited by the predicted crossflow angle profiles.

Acknowledgement

The authors gratefully acknowledge the continued support and encouragement of Mr. M. D. Mack, Supervisor of Flight Controls Technology Research of the Boeing Commercial Airplane Company. Excellent support by the Wind Tunnel Testing and Development group and Systems Technology Instrumentation group is also acknowledged.

References

1. McLean, J.D., and Randall, J.L., "Computer Program to Calculate Three-Dimensional Boundary Layer Flows Over Wings with Wall Mass Transfer," NASA CR-3123, 1978.

2. Humphreys, D.A., "Three-Dimensional Wing Boundary Layer Calculated with Eight Different Methods," AIAA Journal, Vol. 19, No. 2, 1981.

3. Nash, J.F., and Patel, V.C., "Three-Dimensional Turbulent Boundary Layers," SBC Technical Books, 1972.

4. Lighthill, M.J., "On Displacement Thickness," Journal of Fluid Mechanics, No. 4, 1958.

5. Yu, N.J., "Grid Generation and Transonic Flow Calculations for Three-Dimensional Configurations," AIAA Paper No. 80-1391, Presented at Snowmass, Colorado, July 1980.

6. da Costa, A.L., "Application of Computational Aerodynamics Methods to the Design and Analysis of Transport Aircraft," ICAS Paper No. 78-B2-01, September 1978.